nature geoscience

Supplementary information https://doi.org/10.1038/s41561-025-01664-w

Weak asthenosphere beneath the Eurasian interior inferred from Aral Sea desiccation

In the format provided by the authors and unedited

Supplementary Contents

1. Supplementary Text 1 Uncertainty evlauation

2. Supplementary Figures.

Supplementary Fig. 22. 5-year cumulative deformation of DT20 of InSAR observations in eastern Aral Sea, model simulation and the residuals between them.
Supplementary Fig. 23. Cumulative deformation (2016-2020) of InSAR observation and diffusion creep (n=1) models of different Q (activation energy).
Supplementary Fig. 24. Cumulative deformation (2016-2020) of InSAR observation and diffusion creep (n=1) models of different V (activation volume).
Supplementary Fig. 25. Cumulative deformation (2016-2020) of InSAR observation and diffusion creep (n=1) models of different T (temperature).
Supplementary Fig. 26. Cumulative deformation (2016-2020) of InSAR observation and diffusion creep (n=1) models of different d (grain size).

3. Supplementary Tables.
Supplementary Table 1. Summary of published upper mantle Maxwell viscosity estimates from different loading.
Supplementary Table 2. Information of earthquakes with magnitude larger than Mw5.0 in the study area from the GCMT catalogue.
Supplementary Table 3. Information of radar interferograms used in this study.
Supplementary Table 4. Lithospheric and asthenospheric model of the Aral Sea from LITHO1.0.

4. Supplementary References.

1. Supplementary Text 1

InSAR accuracy evaluation

Due to the lack of independent validation data in this region, we evaluate the accuracy of the InSAR measurements from three aspects: 1) The standard deviation of the decomposed vertical displacements within a 5-by-5 km grid, indicating the level of local noise (Extended Data Fig. 3a); 2) The differences in the overlapping areas between ascending and descending tracks (Supplementary Fig. 3) and adjacent parallel tracks (Supplementary Fig. 4); 3) the residuals after the vertical and east-west horizontal decomposition (Extended Data Fig. 2 and Supplementary Fig. 5).

From the spatial variability within 5-by-5 km grid (Extended Data Fig. 3a), the standard deviations are less than 5 mm in most areas, but larger within the Aral Sea, particularly along the coast of remaining water bodies, which may be caused by unwrapping errors and uncompensated tropospheric turbulence. Cross validating the deformation from overlapping tracks is important to evaluate the overall accuracy of InSAR measurements. As the vertical deformation dominates the signal, the difference between the ascending and descending tracks in their overlapping areas is small around the Aral Sea (Supplementary Fig. 3). However, the tracks covering the west (AT86 and DT64) and east (AT115 and DT93) margins show relatively larger difference, resulted from the horizontal motions projected to different lines of sight. The overlapping areas between parallel tracks have large incidence angle differences, making them difficult to compare directly. We thus convert LOS displacement into the vertical direction by assuming that the vertical deformation dominates, and calculate the differences between adjacent parallel tracks in the overlapping regions (Supplementary Fig. 4). They show errors with the root mean square error (RMSE) of 6.64 - 11.47 mm. The largest differences appear on the two ascending tracks (AT86 and AT13) covering the West Aral Sea, probably due to the afternoon acquisition time with stronger atmospheric contributions.

We also calculate the RMSE of residuals after the east-west and vertical decomposition for the six tracks (Supplementary Fig. 5), which are 2.39 mm, 3.30 mm, 2.75 mm, 3.15 mm, 3.17 mm and 1.28 mm of AT86, AT13, AT115, DT64, DT166 and DT93 respectively. These values are all well below the largest cumulative vertical deformation, i.e. ~40 mm, indicating that the vertical deformation we derived is reliable for studying the rheology beneath the surface.

We use regions with three or more overlapping datasets for consistency checking and uncertainty estimation. In such areas, we select triplets (e.g., two ascending and one descending track) from the overlap region. Using two datasets (e.g., one ascending and one descending track), we decompose the deformation, then predict the LOS deformation for the third dataset. The differences between predicted and observed LOS form as estimating uncertainties, with the value of about 2.5 cm in five years (Extended Data Fig. 2).

To evaluate the influence of applying the reference area for flattening interferograms, we apply three reference areas, with decreasing area by 40-by-40 km^2 for each test. We estimate the ramp independently on six different frames, and apply them to the entire interferogram to remove the long wavelength ramp phase for each interferogram. From the decomposed vertical deformation based on the three different reference regions (Supplementary Fig. 6), the smaller the reference area, the greater the deformation. This mainly affects the estimation of viscosity, but its influence is small: $5\pm3\times10^{19}$ Pa s will balance this effect. This is probably because large reference area can better fit long-wavelength orbital errors, particularly in the range direction. It is clear that the large-scale uplift signal can be fitted only by a deep source (> 110 km) with viscosity in the range of 2-8×10^{19} Pa s (Supplementary Fig. 6). The estimation of depth has a smaller impact, as the shallower the ductile layer, the more concentrated the deformation and the larger gradient. Therefore, we calculate the differences between the deformation derived from interferograms with largest and smallest reference areas to indicate the upper bound of the uncertainties due to the ramp correction (Extended Data Fig. 3b).

We further evaluate how the uncertainty propagates from the reference areas to the whole scene. We down-sample the data every 10 km to make them approximately independent, identically distributed random variables. Then, we can assume a diagonal covariance matrix $C_m = (\boldsymbol{G}^T C_d \boldsymbol{G})^{-1}$, where C_d is a diagonal matrix from the variance of the ramp estimation within the reference area, $\boldsymbol{G}$ is the design matrix for the ramp fitting. We then propagate the uncertainties within the reference area to the whole scene for all the long-term interferograms applying $C_{mp} = \boldsymbol{H} C_m \boldsymbol{H}^T$, where $\boldsymbol{H}$ is the design matrix for the whole scene. We average the obtained uncertainty maps to represent the uncertainty levels due to long-wavelength errors for each track (Supplementary Fig. 11). We conduct the same decomposition procedure to obtain the long-wavelength error uncertainties for the vertical deformation (Extended Data Fig. 3c) and for the error bars shown in Fig. 3c.

Additionally, we extracted the deformation of the eastern Aral Sea and the Ordos Block using exactly the same method to demonstrate the reliability of our approach. For the descending trajectory DT20 covering the eastern region of the Aral Sea, we also observe viscoelastic signals that are consistent with showing of the model (Supplementary Fig. 22), but due to the long distance from the Aral Sea, the magnitude is already very small, and the signal-to-noise ratio is relatively low. For the Ordos Block, it is located in the western part of the North China Craton and is one of the core geological units of the North China Craton. The interior of the Ordos Block is stable and rigid without active tectonic structures[58]. GPS data also shows that there is almost no deformation inside it[59]. Our InSAR observation shows the same results, with 5-year cumulative deformation close to 0 mm in LOS direction on most regions (Supplementary Fig. 8).

2. Supplementary Figures.

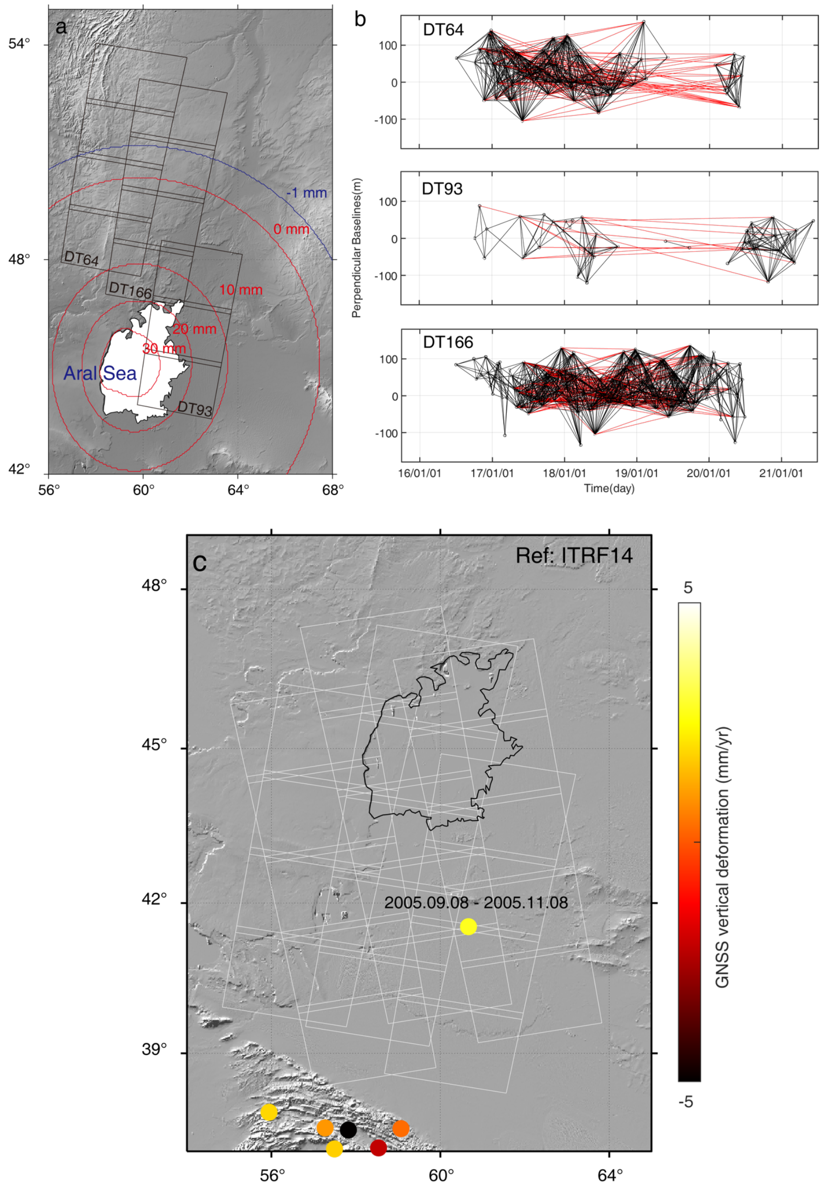

Fig. 1. Schematic diagram of Sentinel 1 satellite data in the northern Aral Sea used in this study. Black rectangles represent footprints of Sentinel-1 images in (a). The red and blue contour lines represent 5-year vertical deformation (2016-2020) simulated by our viscous relaxation model. (b) shows spatial-temporal baselines of the Sentinel-1 SAR images processed with track number indicated to the top left. (c) shows published GNNS stations around the Aral Sea. Source: https://github.com/earjcr1/AHB_GPS Please note that the velocity within the SAR coverage was estimated from only a few time stamps during September to November, 2005, with large uncertainties. Therefore, we did not use it in our analysis.

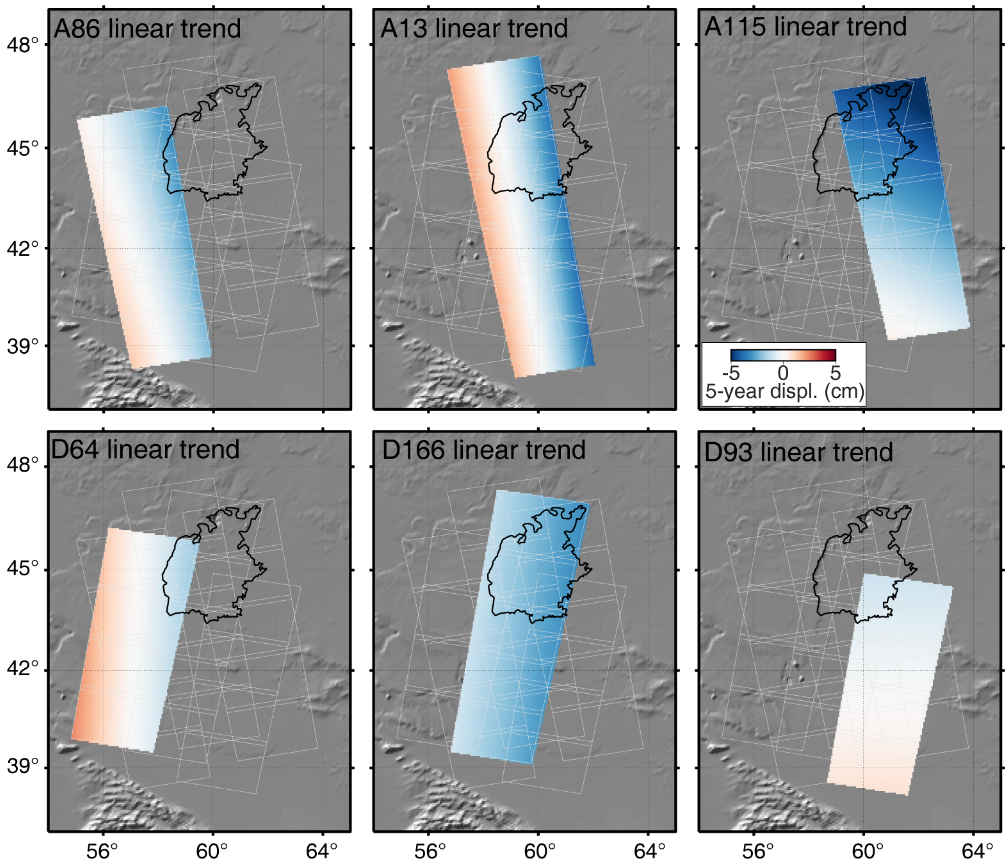

Fig. 2. Estimated and removed linear trend of six tracks using the reference areas as shown in Fig. 3a. Note that deriving the velocity field of the plate in the EU(NNR) reference frame and project this velocity field into the satellite's LOS direction may cause similar trends but with smaller values and simper patterns than fitting the trends from the data.

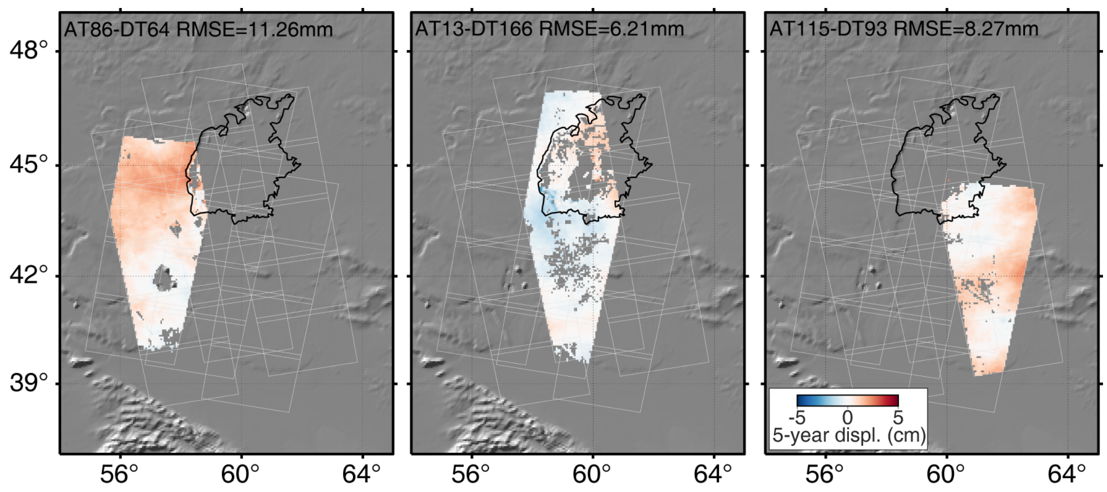

Fig. 3. 5-year deformation difference between overlapping ascending and descending tracks.

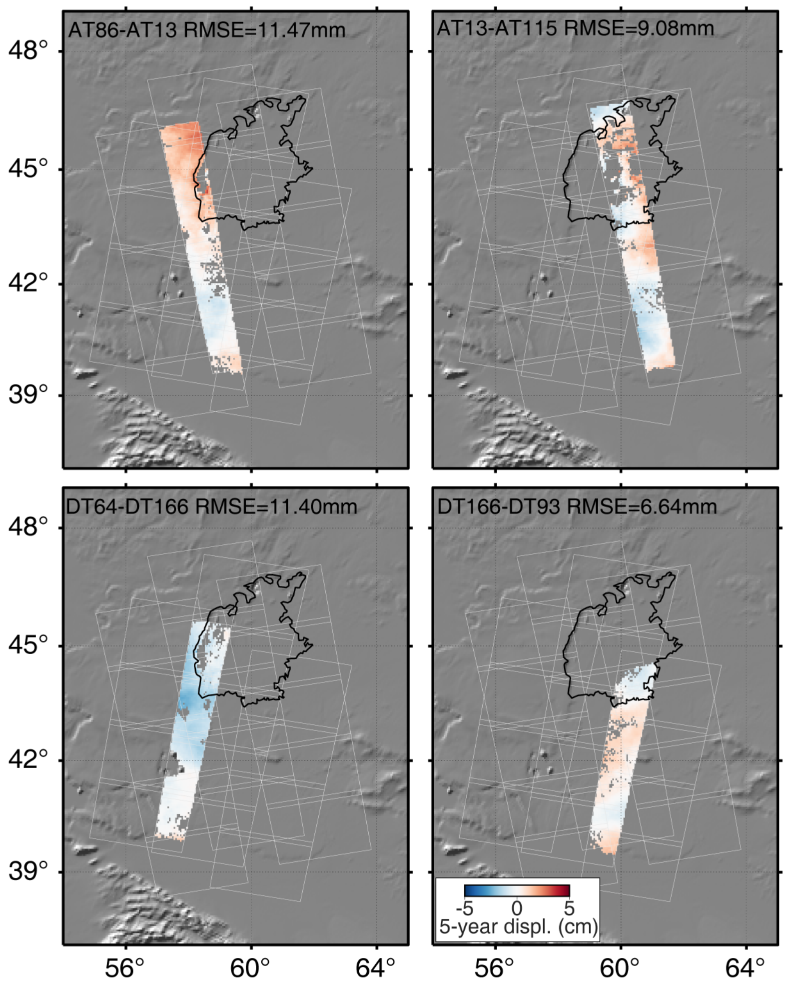

Fig. 4. 5-year deformation difference between adjacent ascending and descending tracks.

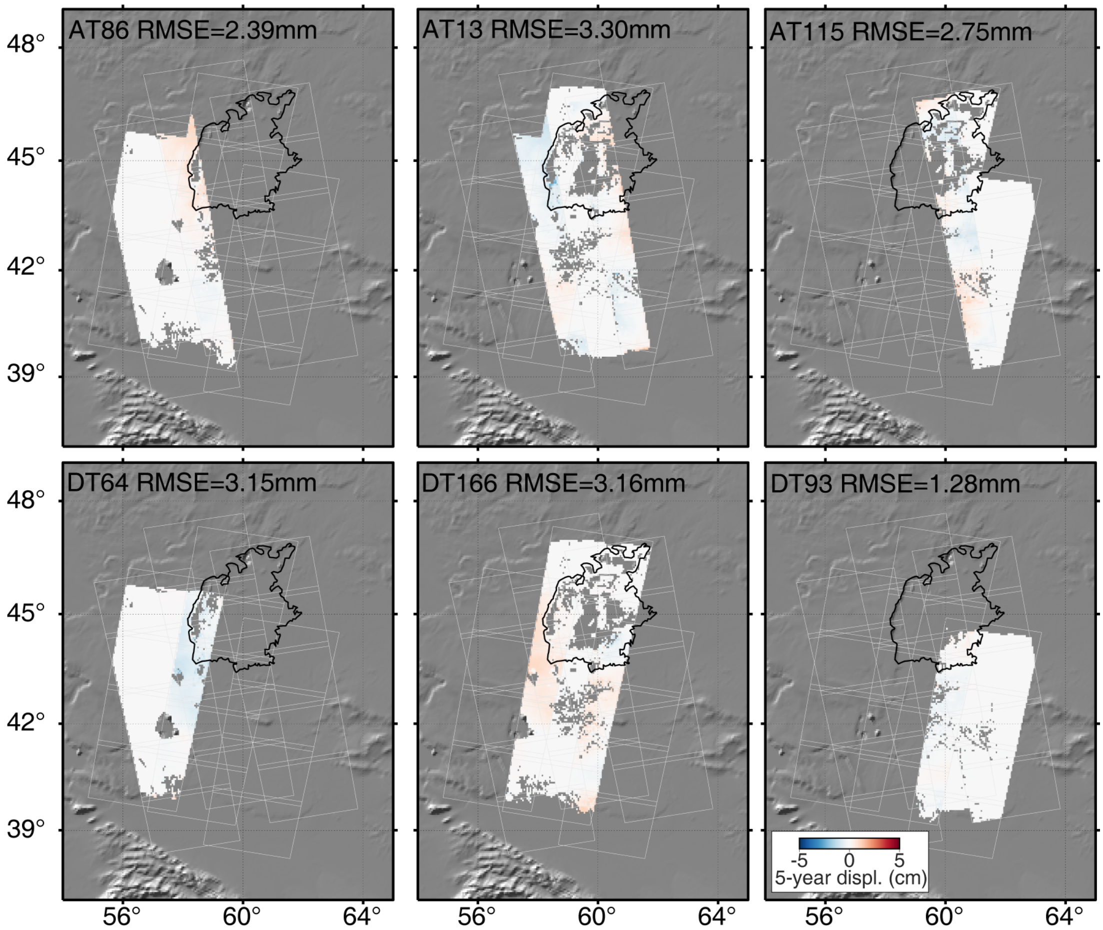

Fig. 5. 5-year residual between the original InSAR observation of six tracks and the deformation calculated based on the decomposition deformation, incidence and azimuth angles.

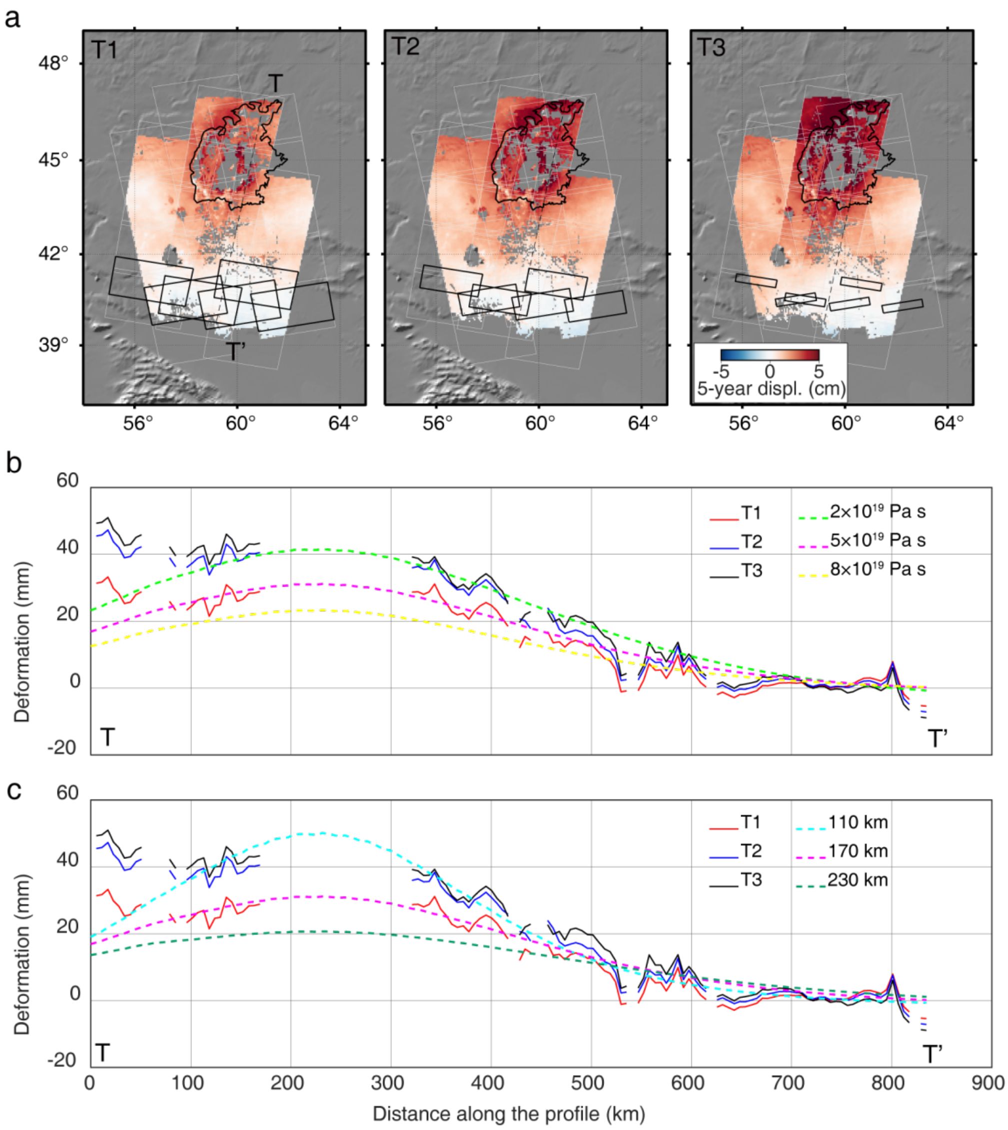

Fig. 6. 5 years vertical cumulative deformation estimated using different reference areas. Black rectangle represents the reference area for different tracks. (b) shows the results of the profiles in (a) and prediction results of models with the same depth (170 km) but different viscosity. (c) shows the results of the profiles in (a) and prediction results of models with the same viscosity (5×10^{19} Pa s) but different depths.

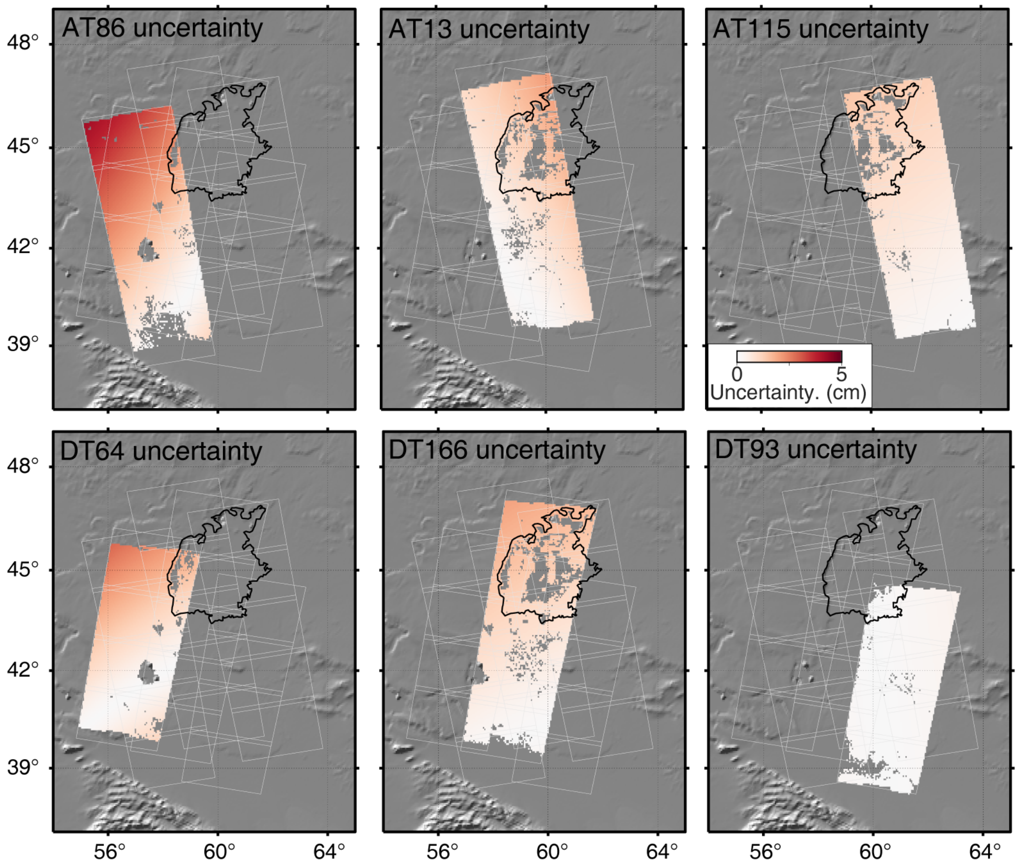

Fig. 7. The differences between the 5 years cumulative deformation using the largest and smallest reference areas. We use these values as the upper bound for the data uncertainties due to long-wavelength errors.

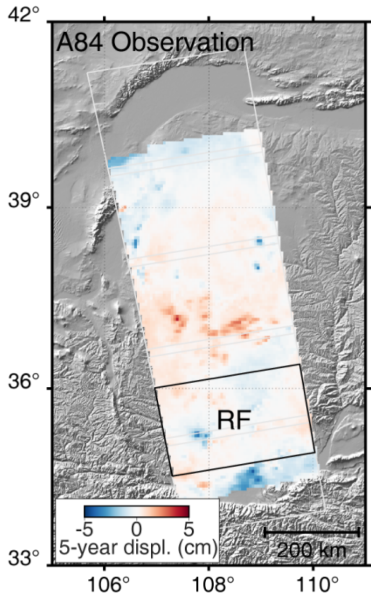

Fig. 8. 5-year cumulative LOS displacements (2017-2021) of the Ordos Block. RF in thick black boxes represents the reference area assuming no deformation. The thin white line represents the location of radar scenes. Warm color means the ground move toward the satellites in the LOS directions.

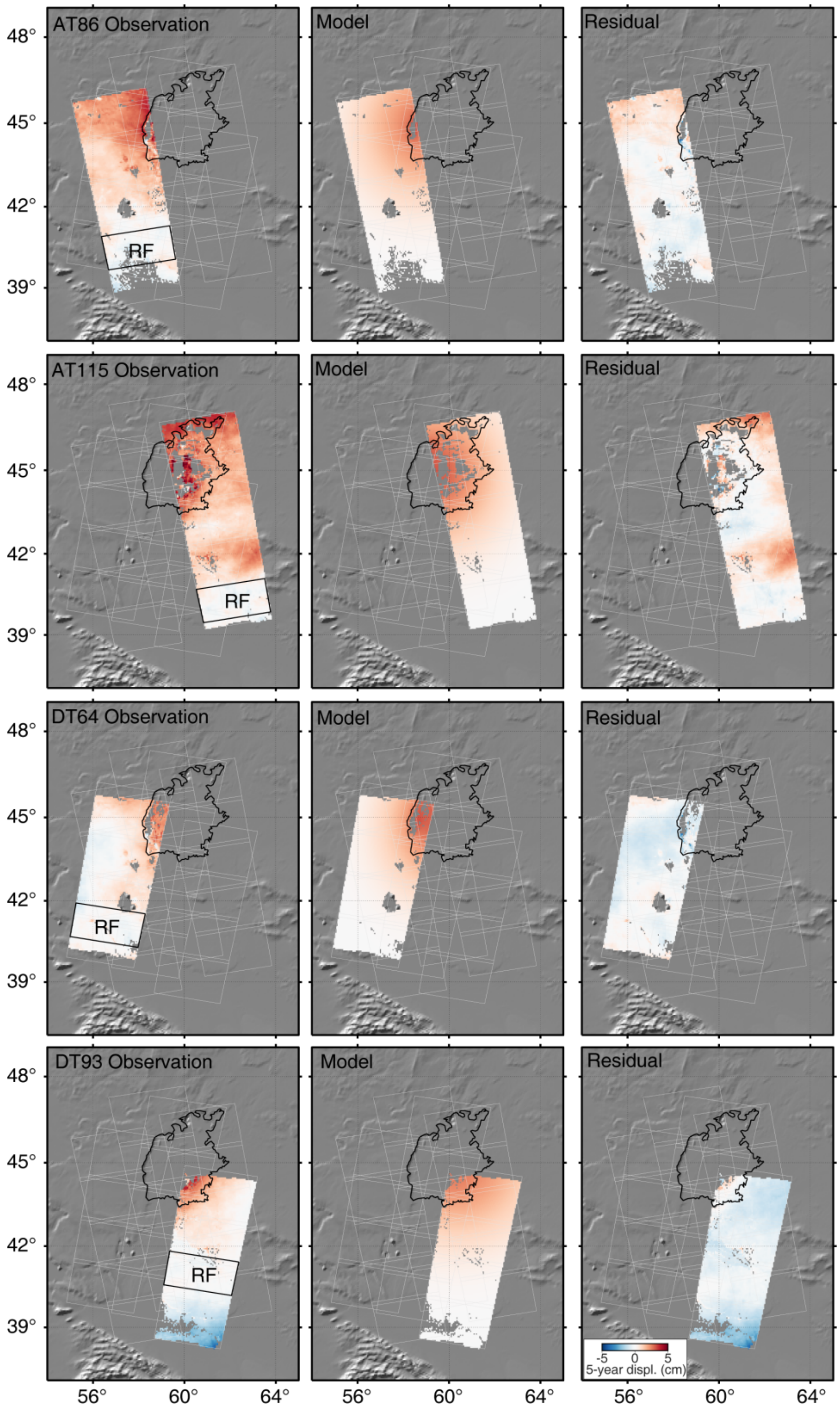

Fig. 9. 5-year cumulative LOS displacements of four tracks of InSAR observations (the other two are show in Fig. 3a), model simulation and the residuals between them. RF in thick black boxes represents the reference area assuming no deformation. The thin white line represents the location of radar scenes and black line shows the boundary of the Aral Sea in 1960. Warm color means the ground move toward the satellites in the LOS directions.

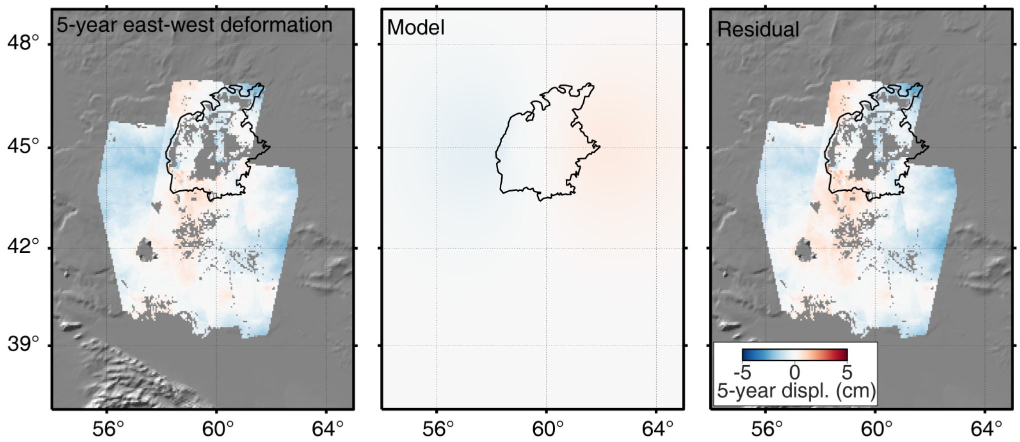

Fig. 10. East-west 5-year cumulative deformation of InSAR and model simulation and the residual. Warm color indicates eastward horizontal movement. Black line shows the boundary of the Aral Sea in 1960. Due to the less sensitive of east-west motion than to vertical motion, the signal-to-noise ratio is too low for model inversion.

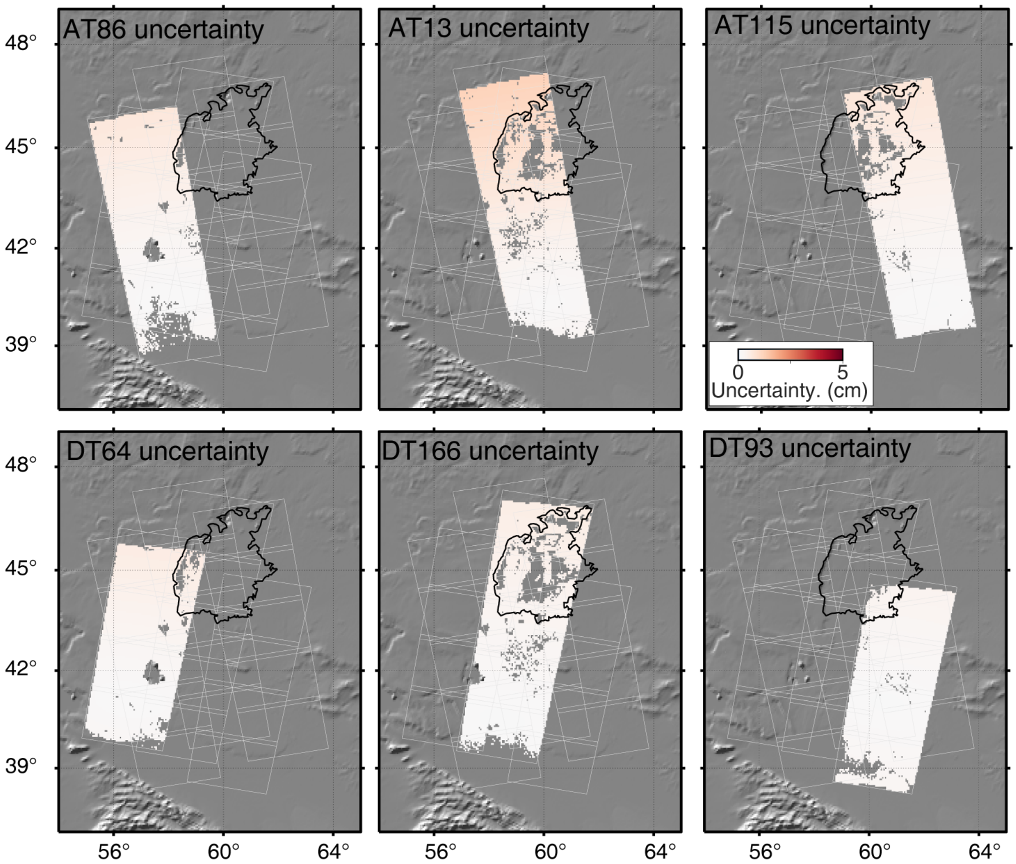

Fig. 11. Propagation of uncertainties due to uncertainties in the ramp calculation in the reference area. We consider these uncertainties in Fig. 3b.

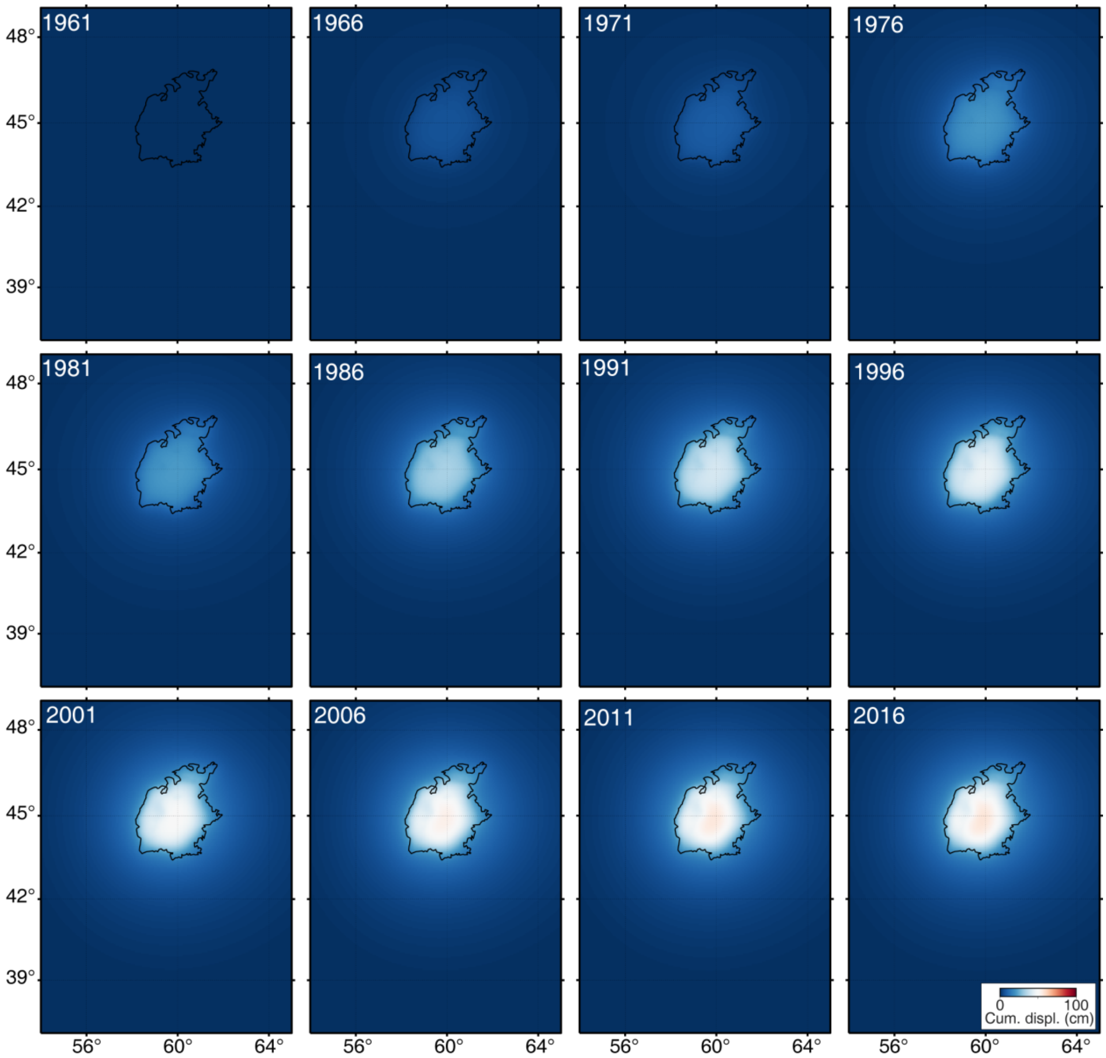

Fig. 12. Simulated vertical cumulative deformation changes of power-law rheology (n=3) of olivine (dry). Warm color indicates uplift movement. Black line shows the boundary of the Aral Sea in 1960.

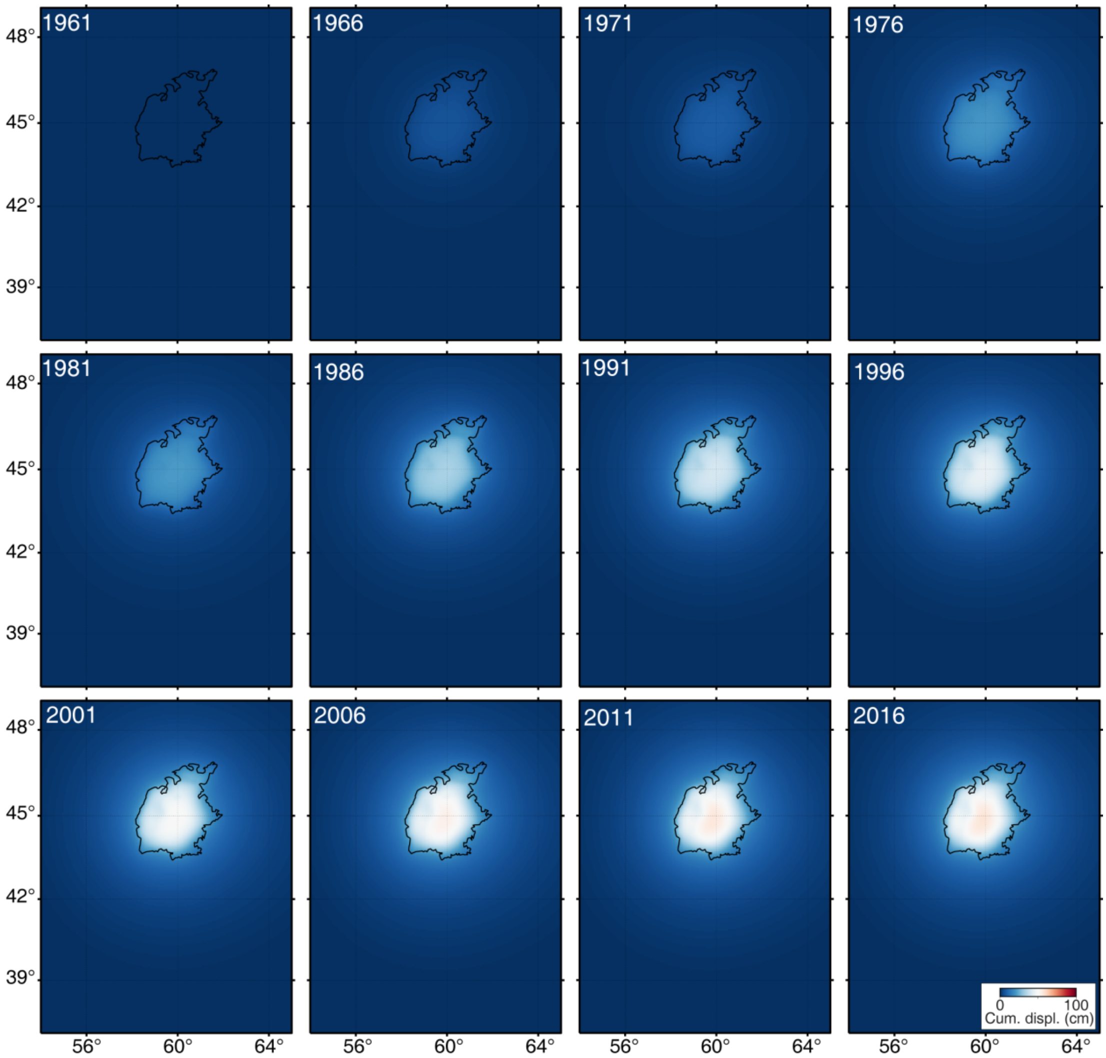

Fig. 13. Simulated vertical cumulative deformation changes of power-law rheology (n=3) of olivine (wet). Warm color indicates uplift movement. Black line shows the boundary of the Aral Sea in 1960.

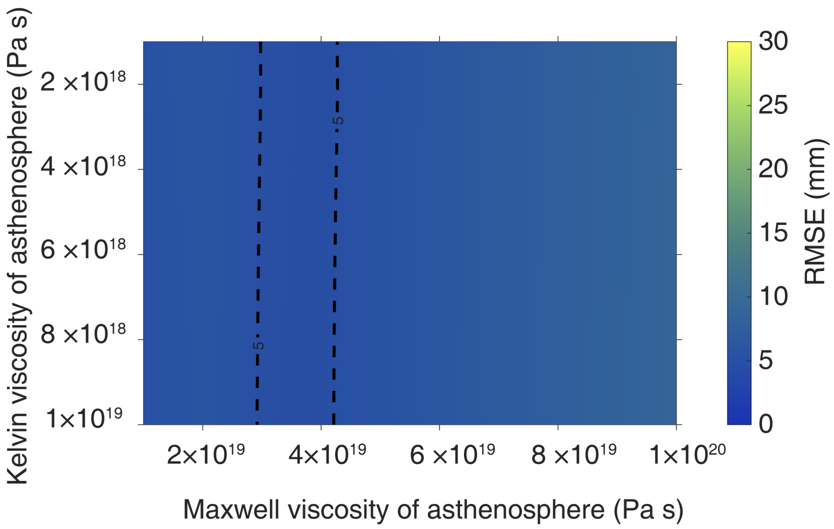

Fig. 14. Misfit between the InSAR observation and the 4-layer viscoelastic model, shown as a function of Maxwell and Kelvin viscosity of the asthenosphere. The color map represents the RMSE of difference of observation and model. The dashed line contours the low misfit area (< 5 mm).

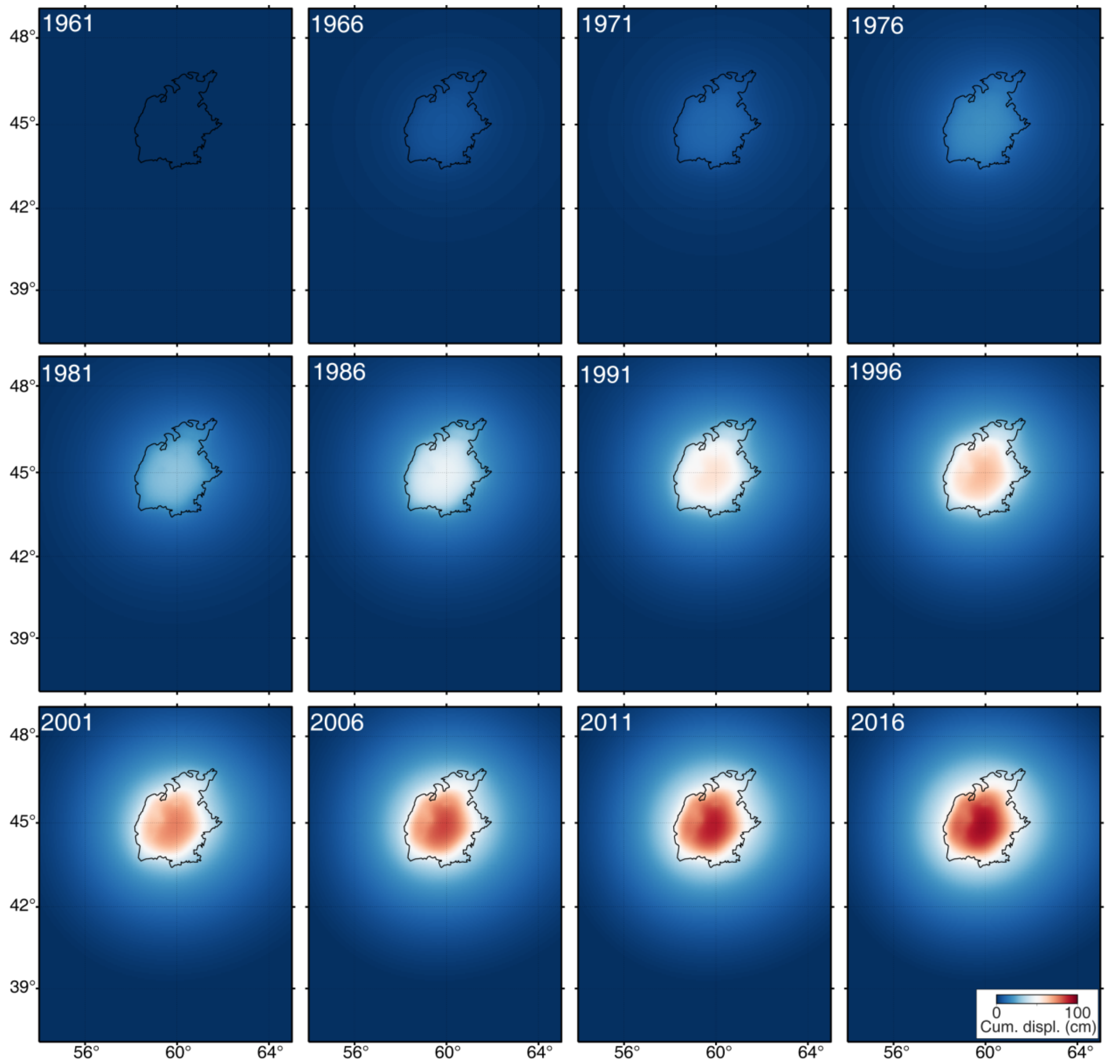

Fig. 15. Simulated vertical cumulative deformation changes with a linear Burgers rheology. Warm color indicates uplift movement. Black line shows the boundary of the Aral Sea in 1960.

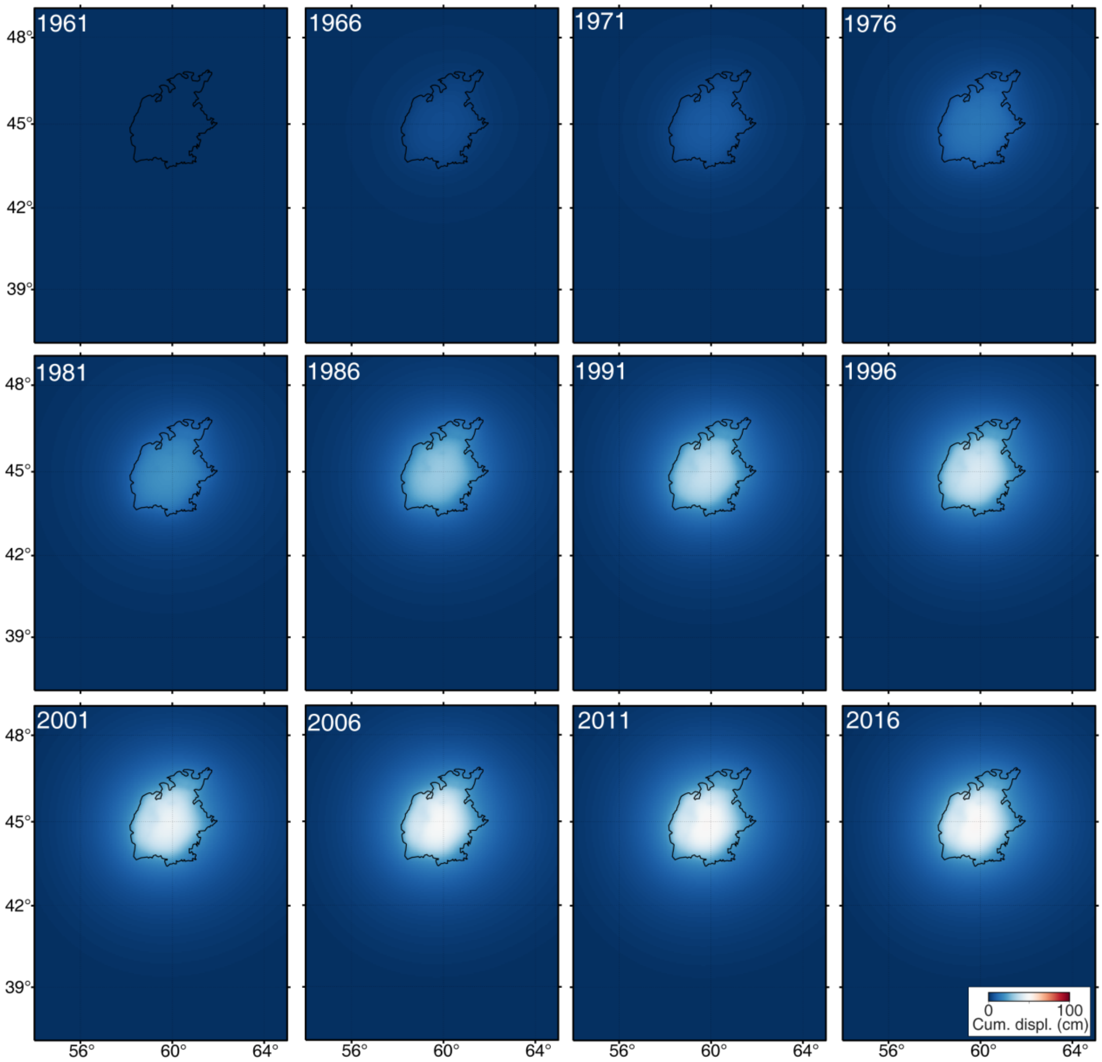

Fig. 16. Simulated vertical cumulative deformation changes of elastic. Warm color indicates uplift movement. Black line shows the boundary of the Aral Sea in 1960.

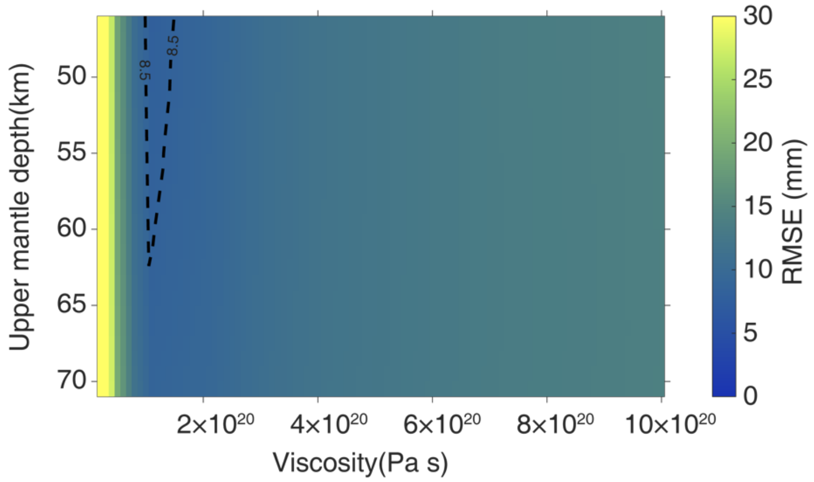

Fig. 17. Misfit between the InSAR observation and the 3-layer viscoelastic model, shown as a function of upper mantle viscosity and depth. The color map represents the RMSE of difference of observation and model. The dashed line contours the low misfit area (< 8.5 mm).

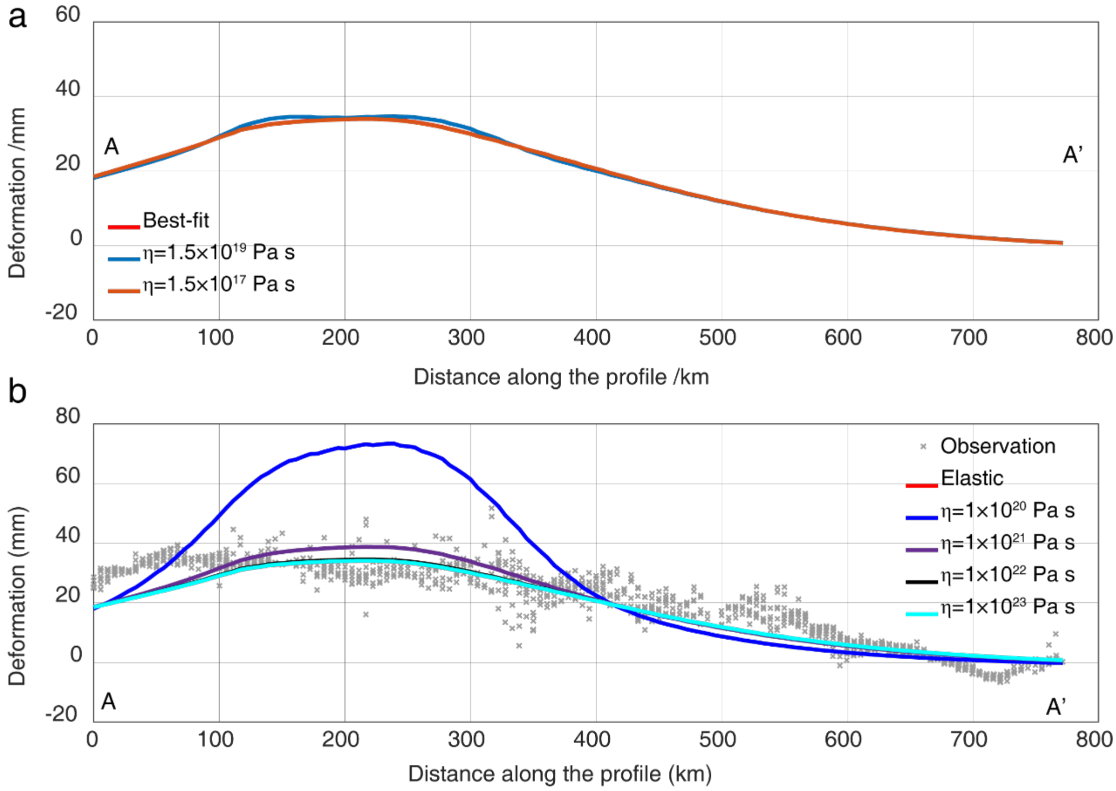

Fig. 18. The profiles of different viscosity of lower crust and lithospheric mantle based on the 4-layer model. (a) The profiles of different viscosity of lower crust (elastic layer at 0-31km, viscoelastic layer at 31-46 km, elastic layer at 46-170km, viscoelastic half space below 170 km with 5×10^{19} Pa s). (b) The profiles of different viscosity of lithospheric mantle (elastic layer at 0-31km, viscoelastic layer at 31-46 km with 1.5×10^{18} Pa s, viscoelastic layer at 46-170km, viscoelastic half space below 170 km with 5×10^{19} Pa s).

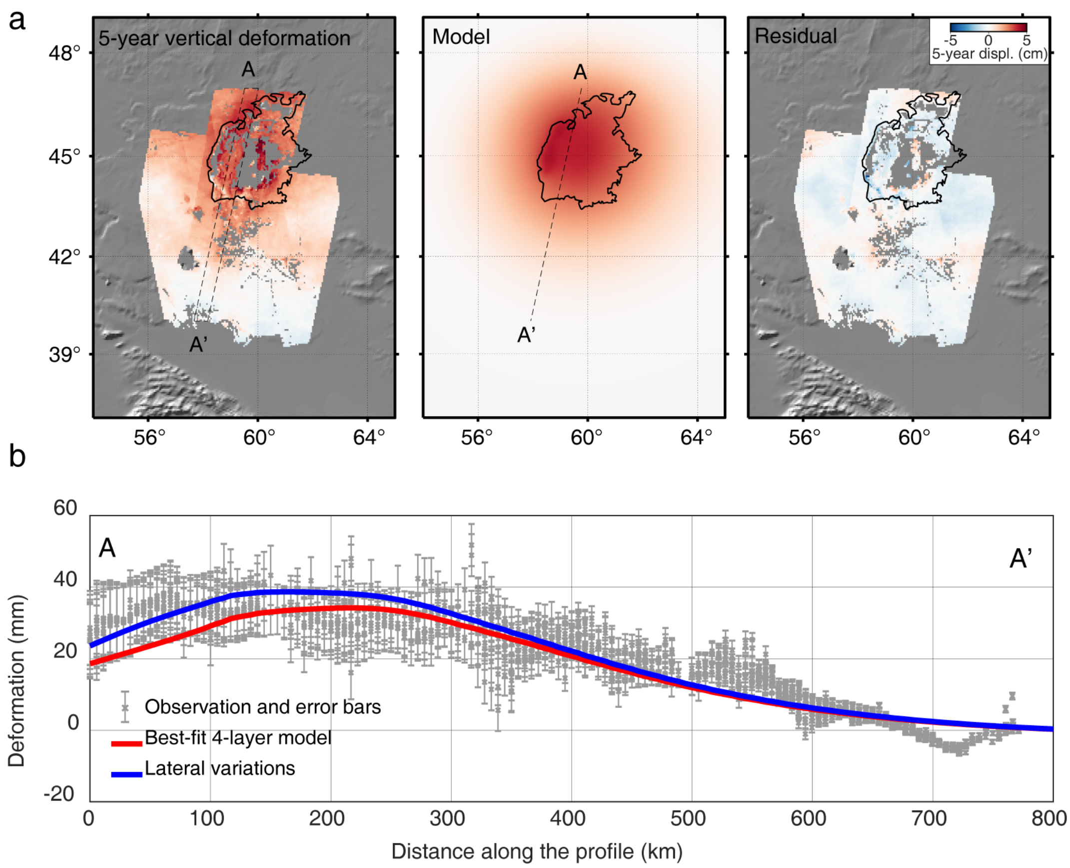

Fig. 19. Cumulative deformation (2016-2020) of InSAR observation and optimal spatial heterogeneity based on 4-layer model. (a) Vertical cumulative deformation with model prediction and residual. Red indicates uplift. (b) Profile of observation and model (dashed areas and lines in (a), superimposed with model of optimal 4-layer model (red). The error bar is the same as in Fig. 3c

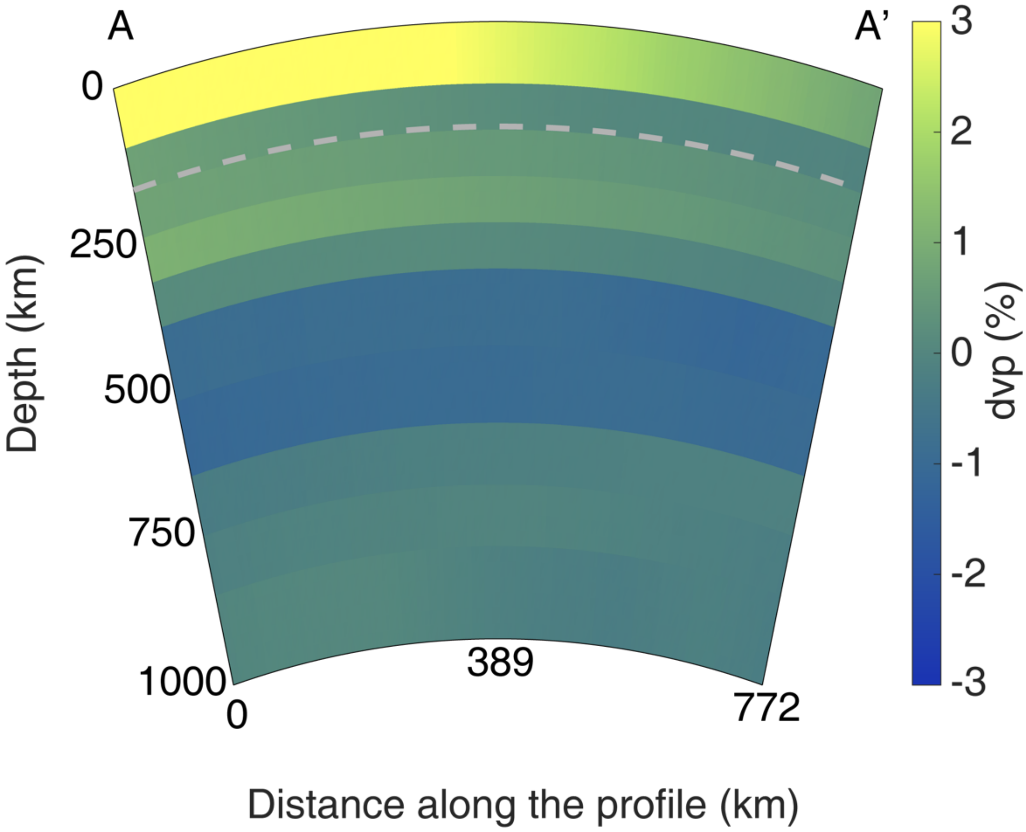

Fig. 20. Vertical section of P-wave velocity anomaly at the same position as Fig. 3c (AA’).

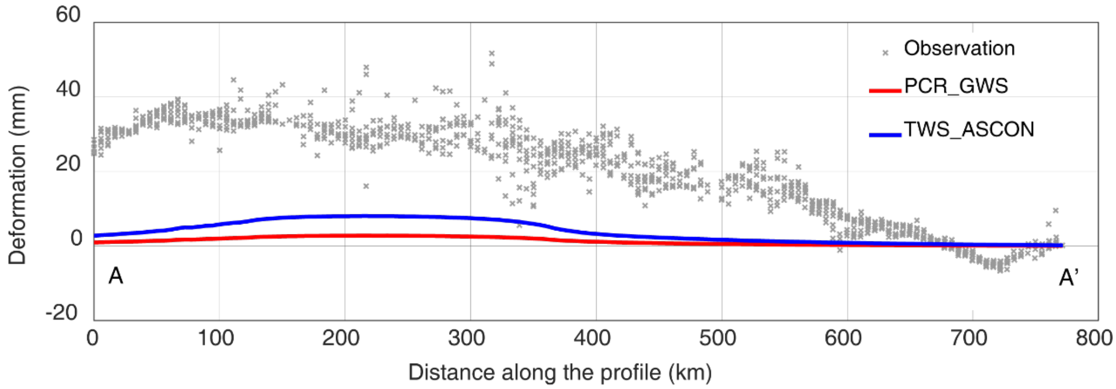

Fig. 21. Cumulative deformation (2016-2020) profiles of InSAR observation and caused by groundwater changes based on the optimal 4-layer model.

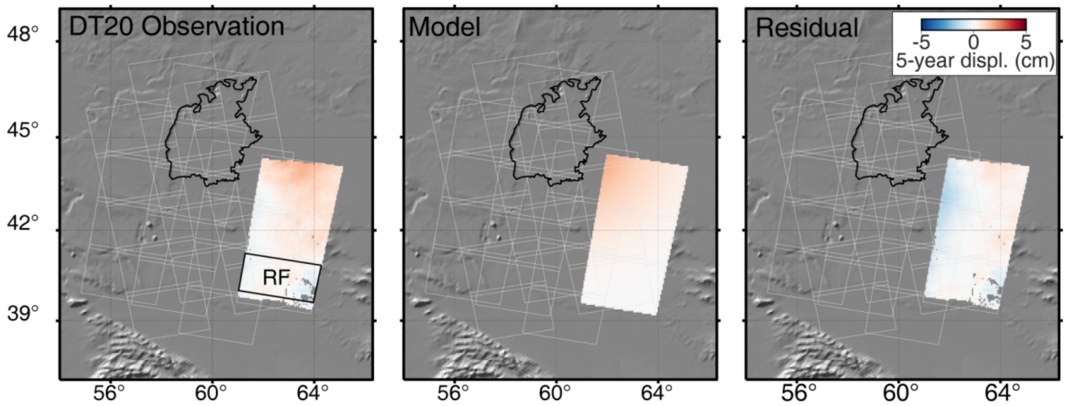

Fig. 22. 5-year cumulative deformation of DT20 of InSAR observations in eastern Aral Sea, model simulation and the residuals between them. RF in thick black boxes represents the reference area assuming no deformation. Black line shows the boundary of the Aral Sea in 1960. Warm color means the ground move toward the satellites in the LOS directions.

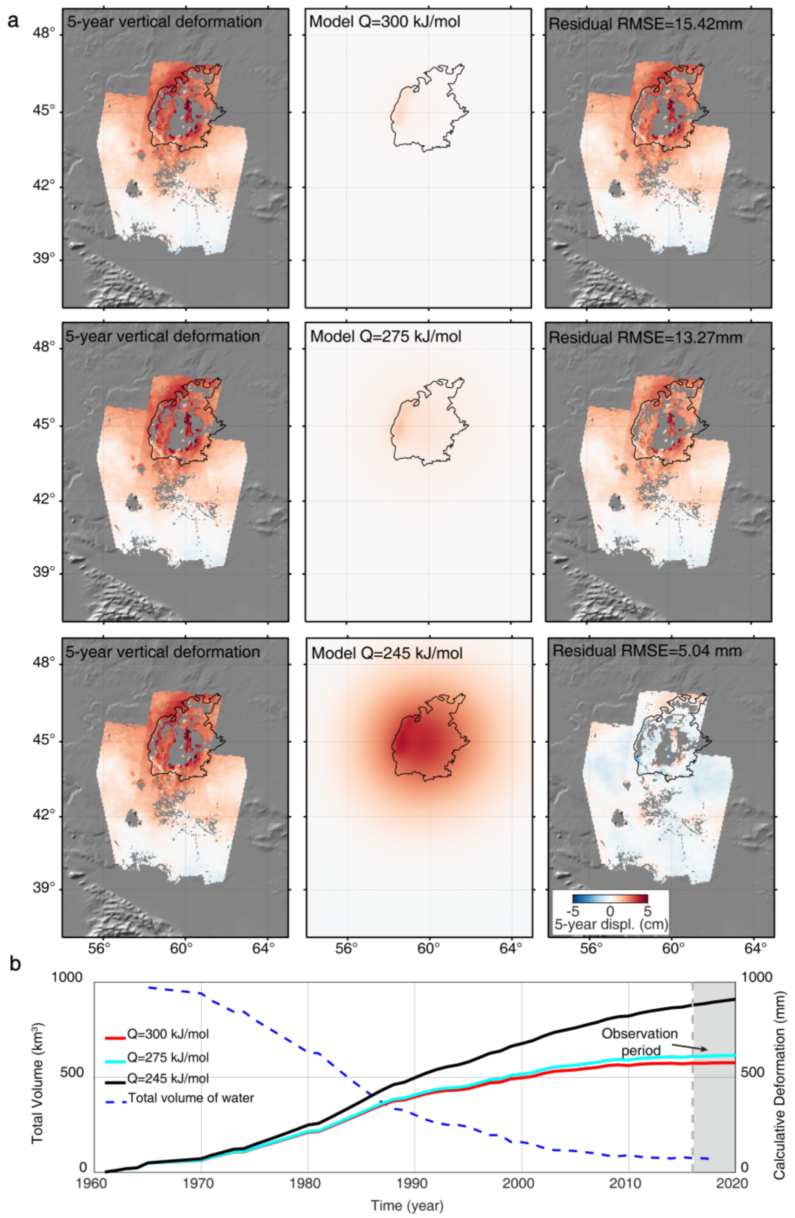

Fig. 23. Cumulative deformation (2016-2020) of InSAR observation and diffusion creep (n=1) models of different Q (activation energy). (a) Vertical cumulative deformation with model prediction and residual. Red indicates uplift. (b) The time-series deformation in the center of the Aral Sea (60° E, 40° N) since 1960 when the regression of the Aral Sea started.

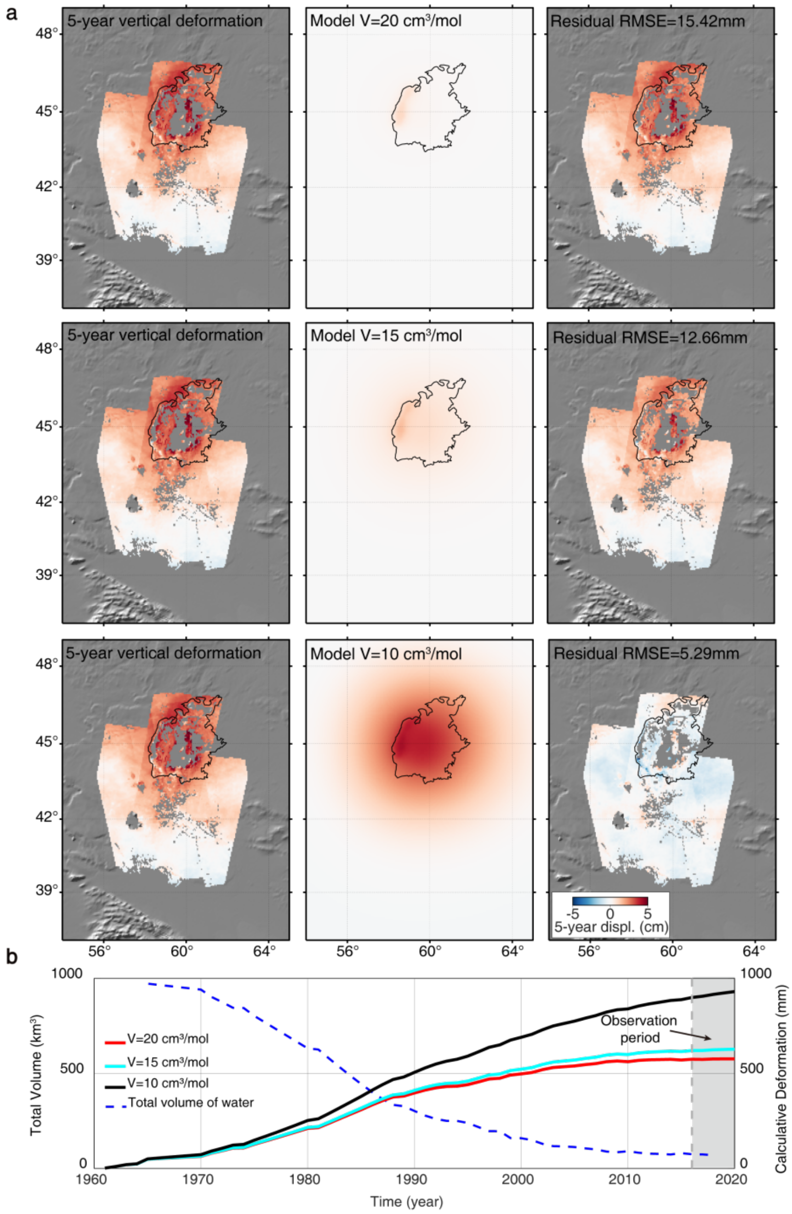

Fig. 24. Cumulative deformation (2016-2020) of InSAR observation and diffusion creep (n=1) models of different V (activation volume). (a) Vertical cumulative deformation with model prediction and residual. Red indicates uplift. (b) The time-series deformation in the center of the Aral Sea (60° E, 40° N) since 1960 when the regression of the Aral Sea started.

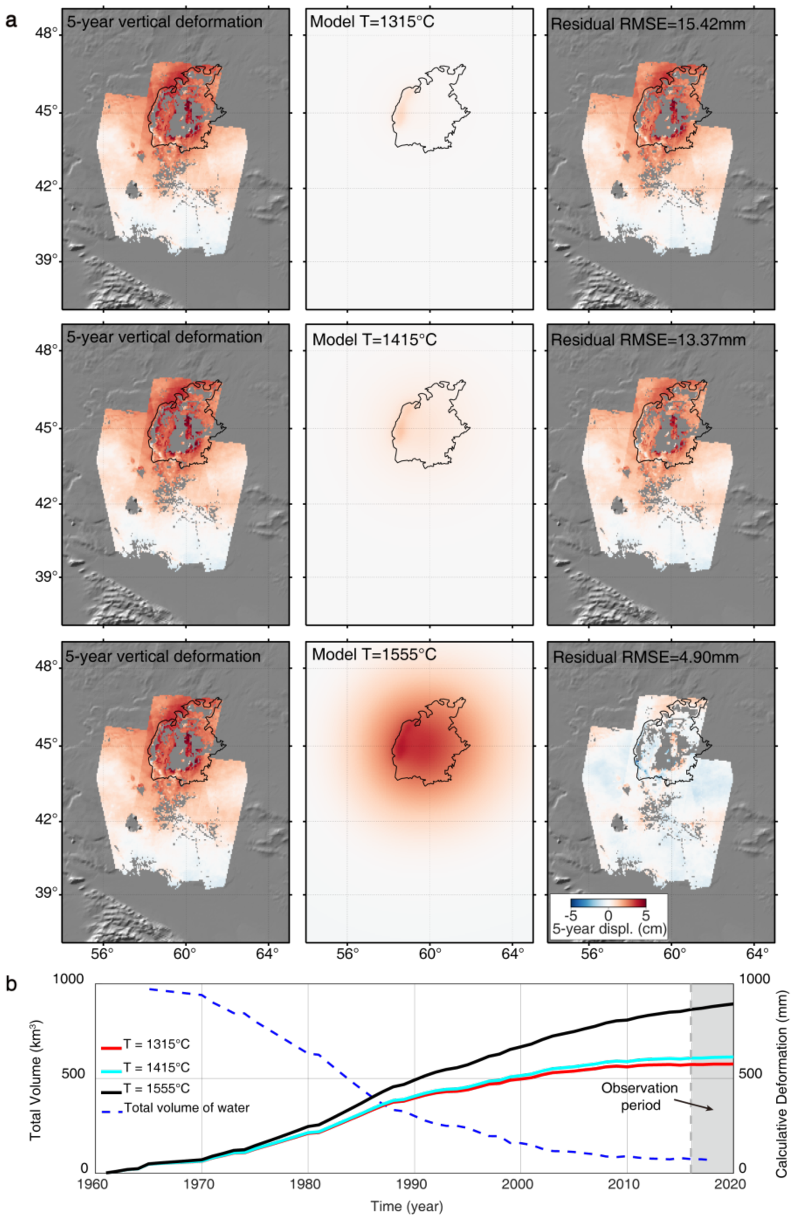

Fig. 25. Cumulative deformation (2016-2020) of InSAR observation and diffusion creep (n=1) models of different T (temperature). (a) Vertical cumulative deformation with model prediction and residual. Red indicates uplift. (b) The time-series deformation in the center of the Aral Sea (60° E, 40° N) since 1960 when the regression of the Aral Sea started.

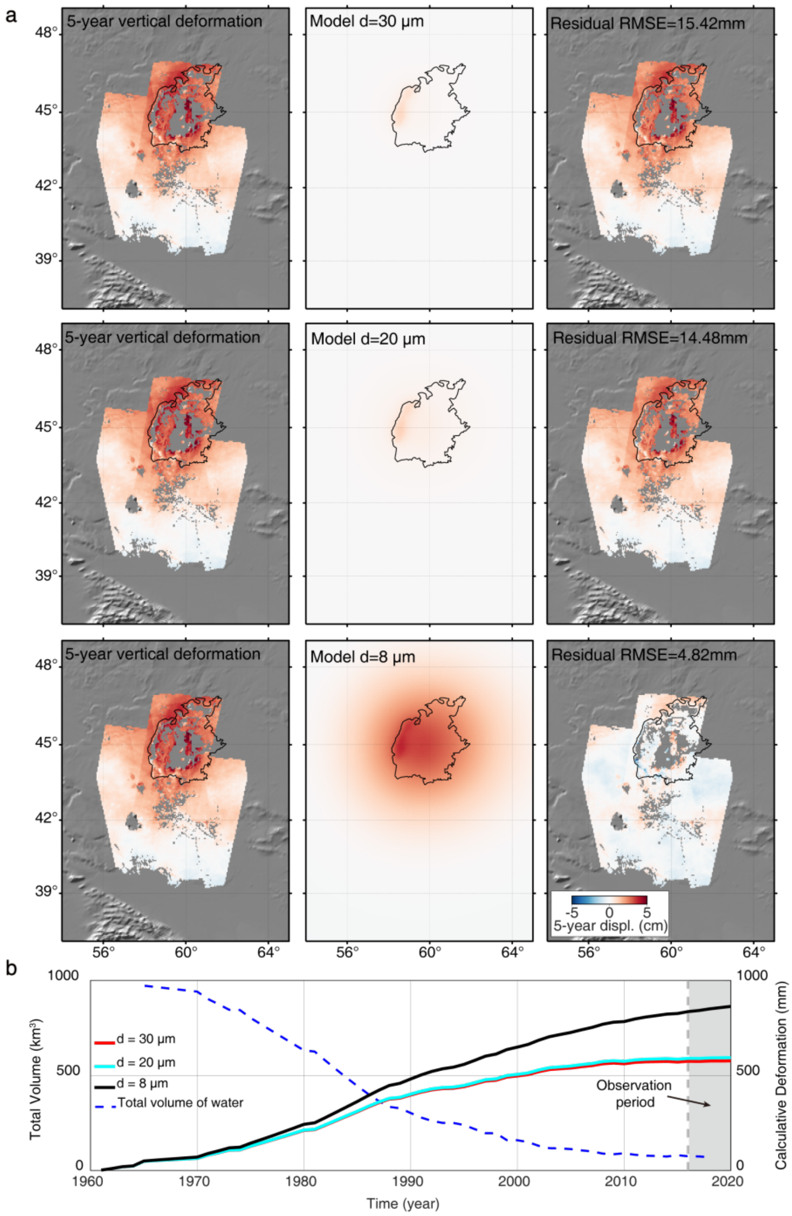

Fig. 26. Cumulative deformation (2016-2020) of InSAR observation and diffusion creep (n=1) models of different d (grain size). (a) Vertical cumulative deformation with model prediction and residual. Red indicates uplift. (b) The time-series deformation in the center of the Aral Sea (60° E, 40° N) since 1960 when the regression of the Aral Sea started.

3. Supplementary Tables.

Table 1. Summary of published upper mantle Maxwell viscosity estimates from different loading.

Viscosity (Pa s)	Depth (km)	Data acquisition period	Method	Location	Lat	Lon	Detail	Source	References
3.0×10^{19}	55	~17 years	GPS	Southeastern Alaska	59.0	-135.0	Mantle asthenosphere	GIA	12
4.0×10^{20}	120	Millennial	Shoreline	Scandinavia	63.5	15.0	Upper mantle	GIA	37
1.0×10^{20}	120	~20 years	Gravity field	Greenland	70.0	-50.0	Upper mantle	GIA	36
1.0×10^{19}	40	~11 years	GPS	Southeastern Iceland	64.0	-19.0	Upper mantle	GIA	60
4.0×10^{18}	60	~13 years	GPS	Western Antarctic	-73.5	-115.0	Upper mantle	GIA	13
2.7×10^{19}	34	Millennial	Shoreline deformation and sea level observations	Southwestern Canada	49.5	-122.5	Upper mantle	GIA	61
3.7×10^{18}	70	~5 years	GPS	Southeastern Alaska	59.0	-137.0	Mantle asthenosphere	GIA	62
1.0×10^{18}	32	~10 years	InSAR	Southern Nevada	36.1	-114.4	Upper mantle	Lakes or reservoirs	63
1.9×10^{19}	35	Millennial	Shoreline deformation	Southern California	32.3	-115.3	Upper mantle	Lakes or reservoirs	64
1.1×10^{18}	30	~48 years	Leveling data	Southern Nevada	36.1	-114.4	Upper mantle	Lakes or reservoirs	65
1.8×10^{19}	25	Millennial	Shoreline deformation	Western Utah	41.0	-112.5	Upper mantle	Lakes or reservoirs	16
3.0×10^{19}	40	Millennial	Shoreline deformation	Western Nevada	39.3	-119.0	Upper mantle	Lakes or reservoirs	38

2.0×10^19	32	~90 years	Leveling data	Central Japan	33.5	133.5	Mantle asthenosphere	Post-seismic	66
7.0×10^19	35	~2 years	GPS	Turkey	40.8	30.0	Upper mantle	Post-seismic	32
5.3×10^18	30	~3 years	GPS	Western Indonesia	2.3	93.6	Mantle asthenosphere	Post-seismic	4
2.5×10^18	50	~5 years	GPS	Western Mongolia	49.4	96.6	Upper mantle	Post-seismic	67
2.0×10^19	31	~27 years	GPS and trilateration	Southeastern Idaho	44.9	112.3	Upper mantle	Post-seismic	68
3.2×10^18	30	~1 year	GPS	Salton Trough	32.7	-115.4	Upper mantle	Post-seismic	69
9.2×10^19	30	~1 year	GPS	Peninsular Ranges	33.0	-117.5	Upper mantle	Post-seismic	69
9.2×10^19	30	~1 year	GPS	Southern Colorado	33.0	-113.0	Upper mantle	Post-seismic	69
3.5×10^18	20	~5 years	InSAR	Southern Iceland	64.0	-20.5	Upper mantle	Post-seismic	70
2.0×10^20	32	~4 year	GPS	Turkey	40.8	30.0	Upper mantle	Post-seismic	71
1.0×10^18	70	~4 months	GPS	Northeastern the Tibet Plateau	30.9	90.6	Upper mantle	Post-seismic	72
2.0×10^20	30	~10 years	GPS	Northeastern Mojave Desert	34.7	-115.7	Mantle lithosphere	Post-seismic	31
4.0×10^19	43	~10 years	GPS	Northeastern Mojave Desert	34.7	-115.7	Mantle asthenosphere	Post-seismic	31
4.0×10^18	43	~10 years	GPS	Southwestern Mojave Desert	33.7	-117.1	Mantle asthenosphere	Post-seismic	31
1.3×10^19	55	~9 years	GPS	Eastern the Tibet Plateau	31.0	103.4	Upper mantle	Post-seismic	9

4.0×10^{18}	30	~8 years	InSAR	Central Nevada	40.5	-117.5	Upper mantle	Post-seismic	73
3.0×10^{19}	30	~3 years	GPS	Chile	-38.1	-73.4	Upper mantle	Post-seismic	74
4.0×10^{18}	38	~28 years	Leveling data	Southeastern Idaho	44.9	-112.3	Mantle asthenosphere	Post-seismic	75
9.0×10^{18}	30	~75 years	Leveling data	Northeastern Japan	39.0	141.5	Upper mantle	Post-seismic	76
2.8×10^{18}	38	~19 months	GPS	Central Alaska	63.5	-147.6	Upper mantle	Post-seismic	77

Table 2. Information of earthquakes with magnitude larger than Mw5.0 in the study area from the GCMT catalogue.

Date	Lon	Lat	Depth (km)	Mw	mb	Ms
19760408	63.65	40.41	15	6.6	6.5	7.0
19760517	63.46	40.42	15	6.7	6.3	7.0
19770714	63.28	40.12	15	5.3	5.5	5.4
19780604	63.13	40.48	10	5.6	6.0	5.1
19840222	54.06	39.55	41	5.8	5.1	5.8
19840319	63.24	40.59	15	7.0	6.5	7.0
19870907	54.87	39.13	29	5.7	5.5	5.5
19921127	59.77	37.36	24	5.3	5.1	5.1
19970204	57.54	37.99	15	5.4	5.3	5.5
19970204	57.5	37.82	15	6.5	5.9	6.8
19970205	57.58	37.84	15	5.2	5.2	5.0
19991119	54.52	37.47	29	5.4	5.3	5.1
20000822	57.57	38.18	15	5.6	5.2	5.8
20001206	54.87	39.6	33	7.0	6.7	7.5
20010610	54.08	39.71	57	5.4	5.5	5.2
20041007	54.32	37.37	32	5.6	5.6	5.4
20050110	54.53	37.46	32	5.3	5.3	5.1
20061012	54.66	39.75	49	5.3	5.5	5.3

Table 3. Information of radar interferograms used in this study. ST means short-term, LT means long-term, Interfs means interferograms.

Track number	Geometry	Time Span yyyymmdd	ST Interfs Generated	ST Interfs Used	LT Interfs Generated	LT Interfs Used
13	Ascending	20151001-20210619	2017	1648	655	323
64	Descending	20151017-20210623	1746	1543	598	439
86	Ascending	20151030-20210624	1994	1556	444	274
93	Descending	20151112-20210625	1822	1686	658	444
115	Ascending	20151113-20210626	1828	1526	428	238
166	Descending	20150930-20210630	1758	1670	663	414

Table 4. Lithospheric and asthenospheric model of the Aral Sea from LITHO1.0.

Layer	Depth (km)	V_s(m/s)	ρ (kg/m3)
Upper crust (including middle crust)	0-31	3600	2800
Lower crust	31-46	4000	3000
Lithospheric mantle	46-127	4700	3300
Asthenospheric mantle	127-	4500	3300

4. Supplementary References.

58. Zhu, S., Chen, J. & Shi, Y. Earthquake potential in the peripheral zones of the Ordos Block based on contemporary GPS strain rates and seismicity. Tectonophysics 824, 229224 (2022).

59. Wang, M. & Shen, Z. K. Present‐day crustal deformation of continental China derived from GPS and its tectonic implications. Journal of Geophysical Research: Solid Earth 125, e2019JB018774 (2020).

60. Árnadóttir, T. et al. Glacial rebound and plate spreading: results from the first countrywide GPS observations in Iceland. Geophys. J. Int. 177, 691-716 (2009).

61. James, T. S., Clague, J. J., Wang, K. & Hutchinson, I. Postglacial rebound at the northern Cascadia subduction zone. Quat. Sci. Rev. 19, 1527-1541 (2000).

62. Larsen, C. F., Motyka, R. J., Freymueller, J. T., Echelmeyer, K. A. & Ivins, E. R. Rapid viscoelastic uplift in southeast Alaska caused by post-Little Ice Age glacial retreat. Earth Planet. Sci. Lett. 237, 548-560 (2005).

63. Cavalié, O., Doin, M. P., Lasserre, C. & Briole, P. Ground motion measurement in the Lake Mead area, Nevada, by differential synthetic aperture radar interferometry time series analysis: Probing the lithosphere rheological structure. Journal of Geophysical Research: Solid Earth 112, (2007).

64. Luttrell, K., Sandwell, D., Smith Konter, B., Bills, B. & Bock, Y. Modulation of the earthquake cycle at the southern San Andreas fault by lake loading. Journal of Geophysical Research: Solid Earth 112, (2007).

65. Kaufmann, G. & Amelung, F. Reservoir‐induced deformation and continental rheology in vicinity of Lake Mead, Nevada. Journal of Geophysical Research: Solid Earth 105, 16341-16358 (2000).

66. MIYASHITA, K. A model of plate convergence in southwest Japan, inferred from leveling data associated with the 1946 Nankaido earthquake. Journal of Physics of the Earth 35, 449-467 (1987).

67. Vergnolle, M., Pollitz, F. & Calais, E. Constraints on the viscosity of the continental crust and mantle from GPS measurements and postseismic deformation models in western Mongolia. Journal of Geophysical Research: Solid Earth 108, (2003).

68. Chang, W. L., Smith, R. B. & Puskas, C. M. Effects of lithospheric viscoelastic relaxation on the contemporary deformation following the 1959 Mw 7.3 Hebgen Lake, Montana, earthquake and other areas of the intermountain seismic belt. Geochemistry, Geophysics, Geosystems 14, 1-17 (2013).

69. Pollitz, F. F., Bürgmann, R. & Thatcher, W. Illumination of rheological mantle heterogeneity by the M7. 2 2010 El Mayor‐Cucapah earthquake. Geochemistry, Geophysics, Geosystems 13, (2012).

70. Jónsson, S. Importance of post-seismic viscous relaxation in southern Iceland. Nat. Geosci. 1, 136-139 (2008).

71. Hearn, E. H., McClusky, S., Ergintav, S. & Reilinger, R. E. Izmit earthquake postseismic deformation and dynamics of the North Anatolian Fault Zone. Journal of Geophysical Research: Solid Earth 114, (2009).

72. Diao, F., Xiong, X. & Wang, R. Mechanisms of transient postseismic deformation following the 2001 Mw 7.8 Kunlun (China) earthquake. Pure Appl. Geophys. 168, 767-779 (2011).

73. Gourmelen, N. & Amelung, F. Postseismic mantle relaxation in the central Nevada seismic belt. Science 310, 1473-1476 (2005).

74. Khazaradze, G., Wang, K., Klotz, J., Hu, Y. & He, J. Prolonged post-seismic deformation of the 1960 great Chile earthquake and implications for mantle rheology. Geophys. Res. Lett. 29, 1-7 (2002).

75. Nishimura, T. & Thatcher, W. Rheology of the lithosphere inferred from postseismic uplift following the 1959 Hebgen Lake earthquake. Journal of Geophysical Research: Solid Earth 108, (2003).

76. Suito, H. & Hirahara, K. Simulation of postseismic deformations caused by the 1896 Riku‐u Earthquake, northeast Japan: Re‐evaluation of the viscosity in the upper mantle. Geophys. Res. Lett. 26, 2561-2564 (1999).
77. Pollitz, F. F. Transient rheology of the upper mantle beneath central Alaska inferred from the crustal velocity field following the 2002 Denali earthquake. Journal of Geophysical Research: Solid Earth 110, (2005).